

Mantle serpentization beneath a failed rift and post-spreading magmatism in the northeastern South China Sea margin

Yutao Liu,¹ Chun-Feng Li,^{1,2} Yonglin Wen,¹ Zewei Yao,¹ Xiaoli Wan,^{3,4} Xuelin Qiu,⁵ Jia-zheng Zhang,⁵ Aqeel Abbas⁶,^{1,6} Xi Peng¹ and Gang Li¹

¹Department of Marine Sciences, Zhejiang University, Zhoushan 316021, China. E-mail: cfl@zju.edu.cn

²Laboratory for Marine Mineral Resources, Qingdao National Laboratory for Marine Science and Technology, Qingdao 266237, China

³State Key Laboratory of Marine Geology, Tongji University, Shanghai 200092, China

⁴Earthquake Research Institute, University of Tokyo, Tokyo 113-0032, Japan

⁵Key Laboratory of Ocean and Marginal Sea Geology, South China Sea Institute of Oceanology, Chinese Academy of Sciences, Guangzhou 510301, China

⁶Earth System Science Programme, Faculty of Science, The Chinese University of Hong Kong, Hong Kong 999077, China

Accepted 2021 January 4. Received 2021 January 1; in original form 2020 September 9

SUMMARY

The post-spreading magmatic activities in the northeastern South China Sea (SCS) margin are very strong, evidenced by widely distributed high-velocity lower crust (HVLC) and numerous volcanoes. However, there are large contrasts in magmatic activities and crustal structure between the Southern Depression (TSD) of the Tainan Basin and the volcanic continental slope area further south. We analyse their crustal *P*-wave velocity structures based on a newly acquired wide-angle ocean bottom seismic data set. The Cenozoic strata below the TSD, a Cenozoic failed rift, are relatively thick (~3–4.5 km) with velocities from 1.6 to 3.6–3.9 km s⁻¹, whereas the Mesozoic strata are relatively thin (~1–2.5 km) with velocities from 4.3 to 4.6–5.2 km s⁻¹. In the TSD, magmatic activities are relatively weak and the crust is severely thinned (~4 km). The crust is 9–15 km thick below the volcanic continental slope area, which shows extensive volcanism. We identified HVLC below the failed rift of the TSD (Zone 1) and attributed it to mantle serpentization, whereas the imaged HVLC below the volcanic continental slope (Zone 3) and HVLC adjacent to the failed rift of the TSD (Zone 2) are due to post-spreading magmatic underplating/intrusions. At the model distance ~90 km, lateral transition from magmatic underplating/intrusions to mantle serpentization occurred abruptly. We concur that post-spreading cooling and thermal contraction in the nearby SCS oceanic lithosphere can trigger decompressive melting and deformation in the thinned continental slope zone. Our study shows that, in addition to mantle serpentization in the continent–ocean transition (COT) zone, mantle can also be serpentized below the rift during early-stage rifting. Weak syn-rifting magmatism and mantle serpentization below the failed rift support that the northeastern SCS has a magma-poor margin.

Key words: Seismic tomography; Continental margins: divergent; Dynamics of lithosphere and mantle.

1 INTRODUCTION

Since the late Mesozoic, the northeastern South China Sea (SCS) has transited from an active subduction of the palaeo-Pacific Plate to continental extension and breakup (e.g. Zhou *et al.* 2006, 2008; Tang & Zheng 2010; Shi & Li 2012; Sun *et al.* 2019). Seafloor spreading in the SCS started at ~34 Ma and stopped at ~15 Ma (Taylor & Hayes 1980, 1983; Briais *et al.* 1993; Li *et al.* 2014).

Two major tectonic zones developed in the northeastern margin of SCS, that is the Tainan Basin to the north and a post-spreading vol-

canic zone in the thinned continental slope to the south. The Tainan Basin contains three subunits, the Northern Depression (TND), Central Uplift (TCU) and Southern Depression (TSD, Li *et al.* 2007; Lin *et al.* 2008). Drilling wells (A-1 and JA-1; Chen 2006) revealed the Mesozoic strata below the TND. Multichannel seismic (MCS) data in the region show tilted fault blocks in the upper crust, and most faults sole downward to quasi-horizontal detachment faults (McIntosh *et al.* 2014; Yeh *et al.* 2012). The TSD is a failed rift not much influenced by post-rifting magmatism (Li *et al.* 2020, Fig. 1).

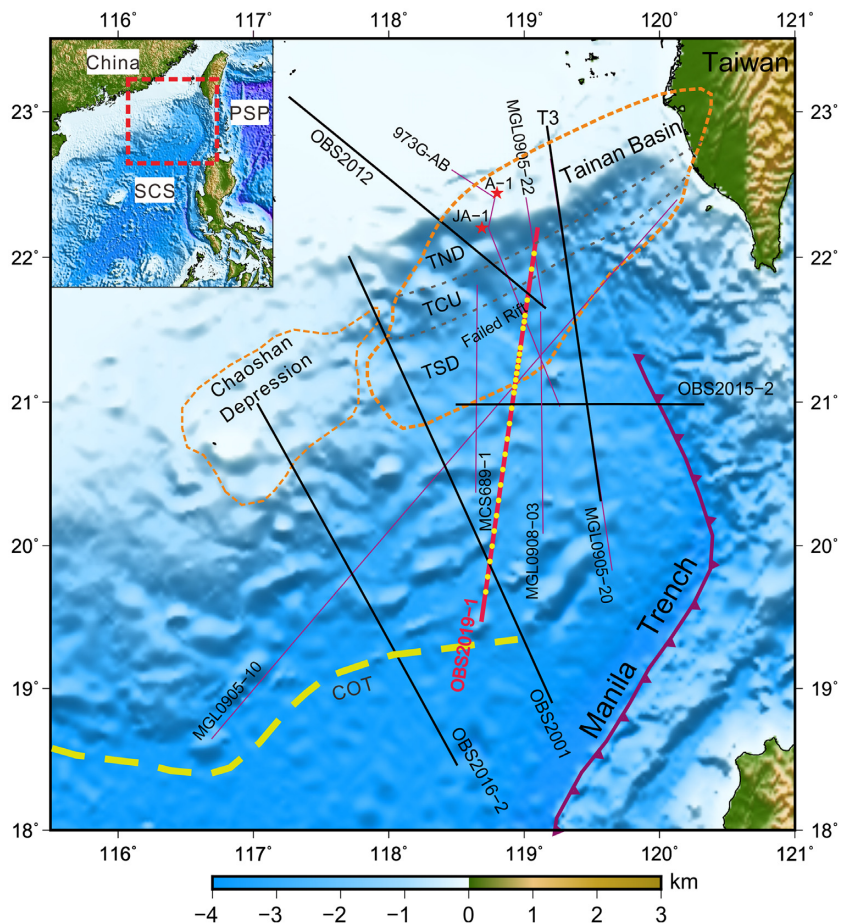


Figure 1. Bathymetry and tectonic structure in the northeastern continental margin of the SCS. The dashed red rectangle in the inset shows the research area. The thin purple lines are MCS profiles from Yeh *et al.* (2012), McIntosh *et al.* (2014) and Li *et al.* (2007). Bold black lines are wide-angle seismic profiles, including OBS2015–2 (Liu *et al.* 2018), T3 (Lester *et al.* 2014), OBS2012 (Wan *et al.* 2017), OBS2001 (Wang *et al.* 2006) and OBS2016–2 (Wan *et al.* 2019). The yellow dashed curve marks the continent–ocean transition zone (COT; Song *et al.* 2019). The red stars show the locations of Wells A-1 and JA-1 (Chen 2006). Our studied profile in this paper is OBS2019–1 (the red bold line), with yellow dots marking position of the ocean bottom seismometers (OBSs). PSP, Philippine Sea Plate; SCS, South China Sea; TND, Northern Depression; TCU, Central Uplift; TSD, Southern Depression.

The northern continental margin of the SCS shows HVLC (Nissen *et al.* 1995; Yan *et al.* 2001; Wang *et al.* 2006; Lester *et al.* 2014; Wan *et al.* 2019) and large-scale volcanic activities (Lüdmann & Wong 1999; Lüdmann *et al.* 2001; Yan *et al.* 2001; Song *et al.* 2017). There are different opinions towards the origin of the HVLC in the region, including magmatic underplating/intrusions (Nissen *et al.* 1995; Yan *et al.* 2001; Wang *et al.* 2006; Zhao *et al.* 2010; Wei *et al.* 2011; Lester *et al.* 2014; Wan *et al.* 2017), mantle serpentinization (Hou *et al.* 2019; Wan *et al.* 2019), and residual material from the subduction of the palaeo-Pacific Plate (Wan *et al.* 2017). The timing of magmatic underplating or intrusions is also debated, either syn-rifting (Nissen *et al.* 1995), or post seafloor spreading (Yan *et al.* 2001; Wang *et al.* 2006; Zhao *et al.* 2010; Wei *et al.* 2011, Wan *et al.* 2019), or from syn-rifting to early spreading (Sun *et al.* 2019).

The origin and formation time of HVLC in the northeastern SCS is key to understanding the process of lithospheric rifting and rupture. In this paper, the structure of thinned continental crust in the northeastern SCS is analysed based on wide-angle reflection/refraction and single-channel reflection seismic data surveyed in 2019. Gravity and magnetic data are also used to further validate the interpretation.

2 SEISMIC DATA ACQUISITION AND PRE-PROCESSING

In 2019, the wide-angle refraction and coincident single-channel reflection seismic line OBS2019-1 was surveyed with R/V Shiyan-2 of South China Sea Institute of Oceanology, Chinese Academy of Sciences. The ~310-km-long NEN-SWS oriented profile extends from the Tainan Basin to the continent–ocean transition zone (Fig. 1).

The array of four Bolt air guns has a total volume of 6000 in³. The length of the single-channel seismic streamer is 300 m. The shooting interval is 90 seconds and a number of 1627 shots were fired. During shooting the cruising speed is about 4 knots, and the shooting interval is about 180 m. Active source OBSs were developed by the Institute of Geology and Geophysics, Chinese Academy of Sciences. A total of 30 OBSs are deployed along line OBS2019–1, but two OBSs (OBS08 and OBS09) lost and another one (OBS03) failed to record data. The spacing between two adjacent OBSs from OBS05 to OBS17 is ~5 km, and for other stations is ~12.5 km (Fig. 1).

After automatic gain control (AGC), bandpass filtering and predictive deconvolution, the single-channel seismic data (Fig. 2) are

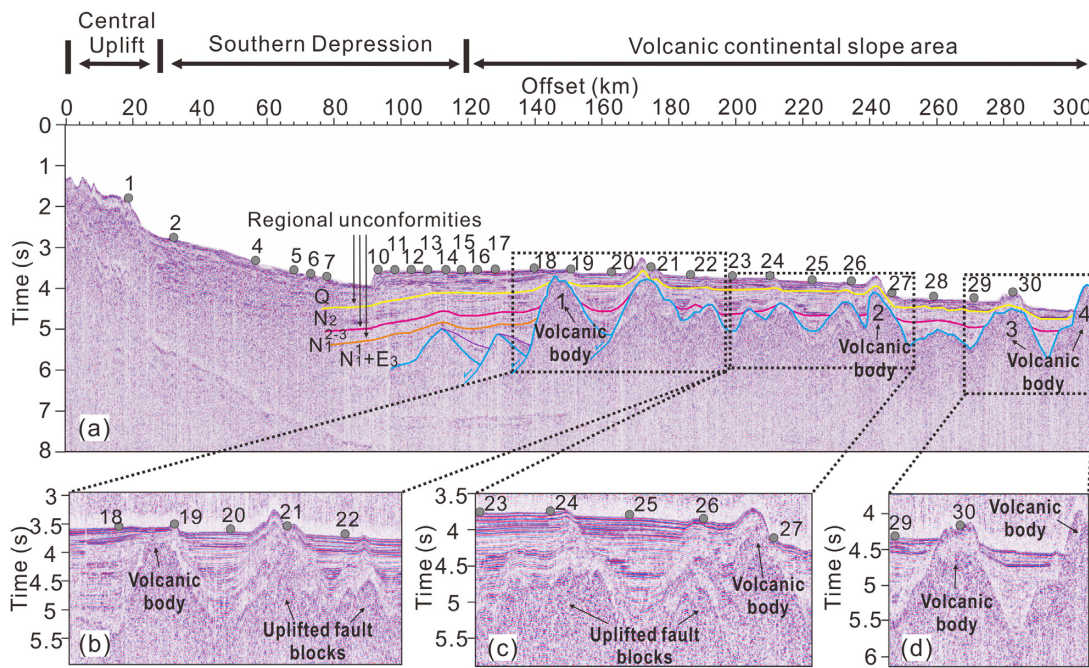


Figure 2. (a) The single-channel reflection seismic profile along line OBS2019-1. (b), (c) and (d) are the close-up views of subsets in (a). The grey dots with numbers are locations of OBSs. The sedimentary sequences are inferred from Li *et al.* (2007).

used for water depth correction and for constraining the initial ray tracing model. The pre-processing of OBS data includes raw data format conversion, clock drifting correction, shot correction and OBS location correction, and noise attenuation. First, the raw data recorded by OBSs are converted into SAC format and then to SEG-Y format. Secondly, time error log files recorded in OBSs are used for clock drifting correction, assuming a linear drift during the data-collection period. Thirdly, shots are relocated according to a distance of 47 m between the GPS and the airgun array. The OBSs are relocated by the Monte Carlo method using the direct water-wave travel time. Finally, bandpass filtering of 3–10 Hz and predictive deconvolution are applied to all OBS data to increase the signal-to-noise ratio.

3 VELOCITY MODELS

3.1 Ray tracing forward modelling

The basement of TSD is not well imaged on the single-channel seismic profile, and in building the initial *P*-wave velocity model, we also referred to other published seismic data nearby (e.g. Chen & Jaw 1996; Chen 2006; Wang *et al.* 2006; Li *et al.* 2007; Tang & Zheng 2010; Yeh *et al.* 2012; Lester *et al.* 2014; Wan *et al.* 2017; Liu *et al.* 2018; Wan *et al.* 2019, Fig. 6b). There are two types of crustal models in published papers. One has two units (upper crust and lower crust, e.g. Wan *et al.* 2019), and another has three units (upper crust, lower crust and high-velocity lower crustal layer, e.g. Liu *et al.* 2018). In ray tracing forward modelling, we firstly tried a two-layer initial crustal model. But we found it difficult to fit Pg phases in the TSD due to velocity gradient variation in the lower crust. In addition, we found reflections from the top of high-velocity lower crustal layer in the OBS records and multichannel seismic profiles (Yeh *et al.* 2012; McIntosh *et al.* 2014). Therefore, we added a high-velocity lower crustal unit in our initial model. The initial velocity model is shown in Fig. 6(b).

Refracted and reflected seismic phases listed in Table 1 were identified by software Rayinvr (Zelt & Smith 1992). In fact, Pg phases include refractions from the upper crust, lower crust and high-velocity lower crustal layer. In the ray tracing modelling, it is difficult to identify different Pg phases because there is no significant difference in velocity slope of different Pg phases. So we used the same colour to represent different Pg phases for convenience.

Ps3 phases are found at model distance 0–140 km on line OBS2019-1 (OBS01–OBS18), and their extents towards the sea become shorter (Fig. 6e), indicating a gradual seaward thinning of the Cenozoic strata. Ps4 phases exist in the TSD (60–120 km, OBS05–OBS15), with apparent velocities of ~4.25–4.75 km s⁻¹ (Fig. 6e). Pg phases exist in all OBS records, and their extents in the TSD are relatively short (OBS01–OBS11), reflecting the much thinned crust (Fig. 6d). Further seawards, the extents of the Pg phases become longer (OBS12–OBS29), revealing thicker crustal thickness, than in the TSD (Fig. 6e). Pn phases in the Tainan Basin show apparent velocities of ~7.75–8.25 km s⁻¹. In the Tainan Basin, it is difficult to distinguish between Pn and Pg phases, and there are no PmP phases (e.g. Figs 3 & 4), indicating possible mantle serpentinization that dimmed the mantle reflections. The interface between the Cenozoic and Mesozoic strata is sharp, and Ps3P phases are mainly distributed in the Tainan Basin (e.g. Fig. 3). PmP and PhP phases are mainly distributed in the seaward side of the survey line (e.g. Fig. 5). OBS20 shows PmP and PhP phases with different arrival time and slopes (Fig. 5). Specific seismic records and ray tracing results of other 24 OBSs are provided in the supplementary materials (Figs S1–S24).

Picking uncertainties for phases Pw, Ps2P, Ps3P, Ps4P, Ps3 and Ps4 are 50 ms, and for phases Pg, Pn, PmP and PhP are 90 ms (Table 1). These uncertainties reflect variations in signal-to-noise ratio and instrument response, and are used to define error tolerances for traveltome tomography. In the final forward model, a total of 22 648 refraction and reflection arrivals were picked up from 27 OBSs data, and the normalized χ^2 for evaluating the fitting goodness between

Table 1. Abbreviations for identified seismic phases.

Phase	Symbol
Direct water-wave	Pw
Refraction from the Cenozoic sedimentary layer	Ps3
Refraction from the Mesozoic sedimentary layer	Ps4
Refraction from the crust and high-velocity lower crust anomalies	Pg
Refraction from the upper mantle	Pn
Reflection from the bottom of the second Cenozoic sedimentary layer	Ps2P
Reflection from the Cenozoic basement	Ps3P
Reflection from the Mesozoic basement	Ps4P
Reflection from the Moho	PmP
Reflection from the top of high-velocity lower crustal bodies	PhP

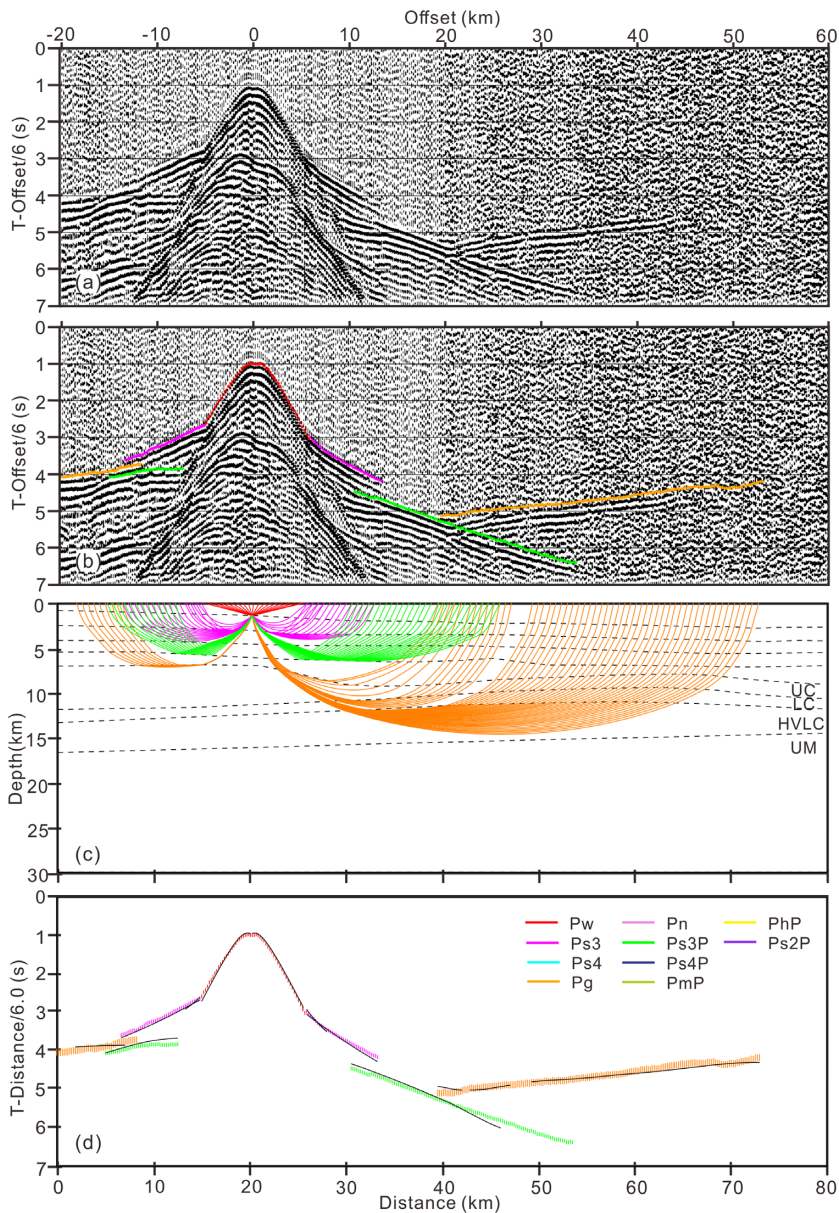


Figure 3. (a) Original seismic records of the vertical component of OBS01 with a reduction velocity of 6.0 km s^{-1} . (b) Picked phases of original seismic records. (c) The ray tracing paths. Ray paths in different colours correspond to different phases in (d). (d) The traveltime fitting (black) of picked phases.

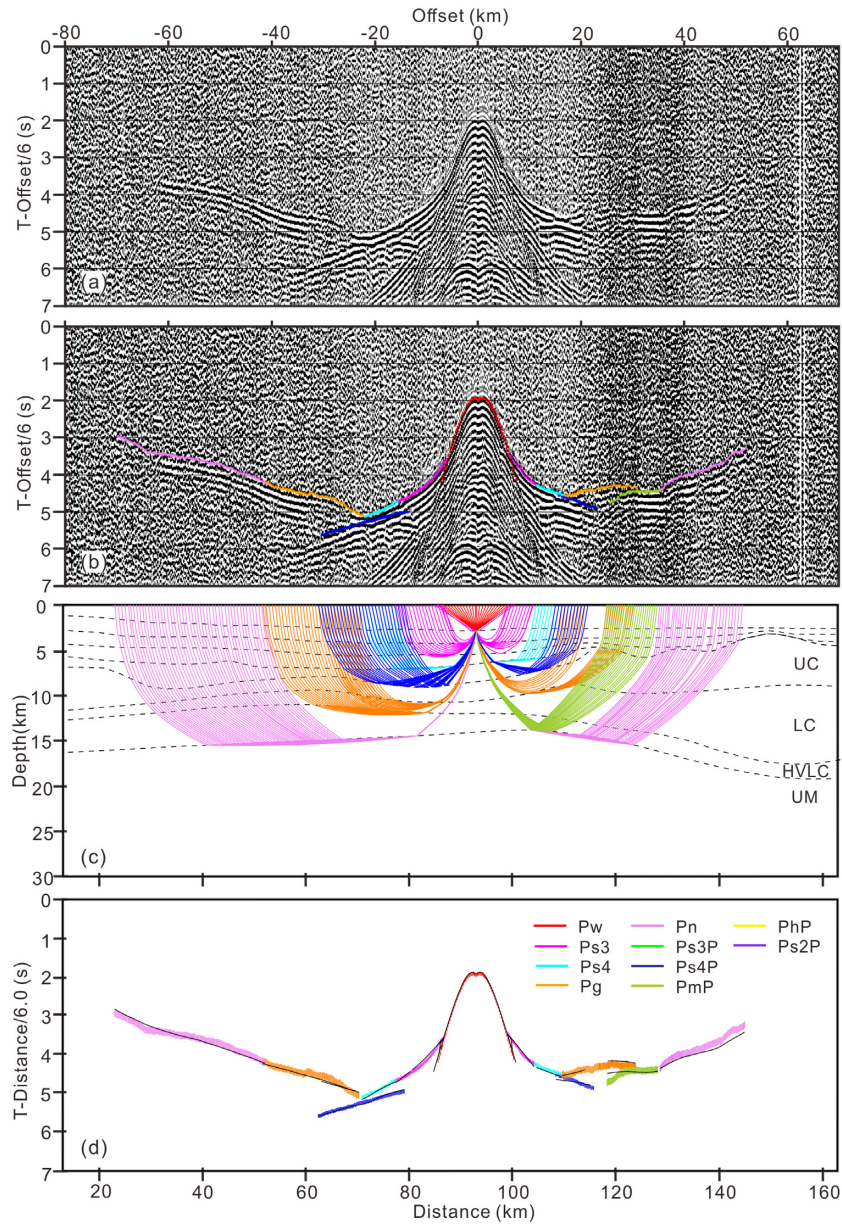


Figure 4. (a) Original seismic records of the vertical component of OBS10 with a reduction velocity of 6.0 km s^{-1} . (b) Picked phases of original seismic records. (c) The ray tracing paths. Ray paths in different colours correspond to different phases in (d). (d) The traveltime fitting (black) of picked phases.

the simulated and the observed data is 1.25 (Table 2), close to the optimal value of 1.0. The root-mean-square error (RMS) is 89 ms.

The ray coverage is rather dense (Fig. 6d), giving a high reliability of the final forward model. In the final forward model (Fig. 6c), reflections from the top of high-velocity lower crustal layer are distributed at model distances 75–85 km, 175–200 km and 240–247 km along the velocity profile. There is no PhP reflection from the top of the high-velocity lower crustal layer at model distance 130–160 km. Moreover, the velocity of HVLC is less than 7.0 km s^{-1} at model distance 130–160 km. Thus, this layered structure could be biased. There could be no single layer, but some discrete high-velocity lower crustal zones. We remained the reflected interface constrained by PhP at the top of high-velocity lower crustal zones. The final ray tracing model (Fig. 6c) reveals several high-velocity lower crustal anomalies ($>7.0 \text{ km s}^{-1}$). The high-velocity lower crustal anomaly below the TSD has higher velocities ($7.0\text{--}7.8 \text{ km s}^{-1}$; 30–70 km)

than other high-velocity lower crustal anomalies ($7.0\text{--}7.3 \text{ km s}^{-1}$; 170–270 km) on the profile.

3.2 Tomographic inversion

Compared with the trial-and-error forward modelling, inversion provides objective estimations of resolution, uncertainty and non-uniqueness (Zelt & Smith 1992). The initial velocity structure of sedimentary layers in the inversion comes from the final ray tracing forward model (Fig. 6c). The velocity increases linearly from 5.2 to 8.2 km s^{-1} from the top of upper crust to the bottom of the initial model, and the initial Moho depth is a constant of 15 km (Fig. 7a). The picked travel time of Pg, Pn and PmP arrivals are used as the input data. The joint refraction and reflection travelttime inversion code Tomo2D (Korenaga *et al.* 2000) is used to obtain the 2-D P-wave velocity model and the Moho geometry. The horizontal and

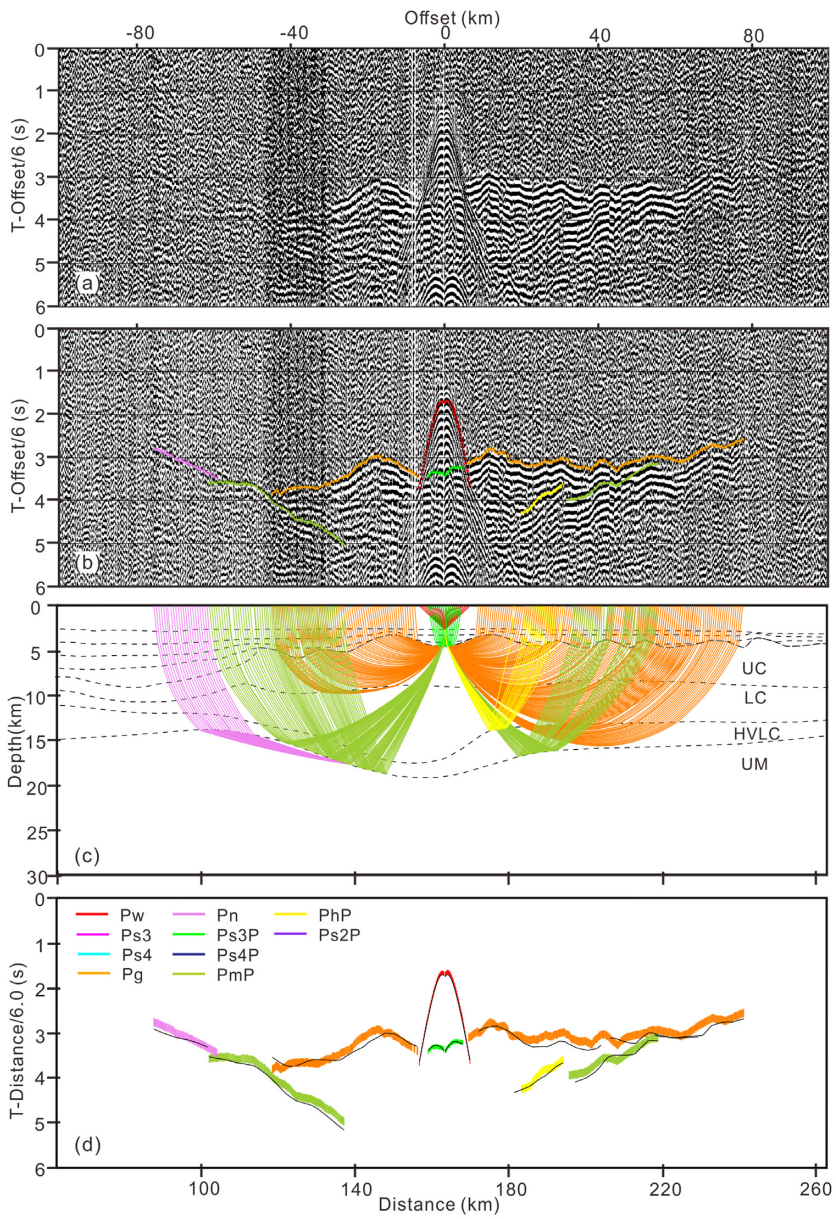


Figure 5. (a) Original seismic records of the vertical component of OBS20 with a reduction velocity of 6.0 km s^{-1} . (b) Picked phases of original seismic records. (c) The ray tracing paths. Ray paths in different colours correspond to different phases in (d). (d) The traveltime fitting (black) of picked phases.

Table 2. Number of picks, RMS and χ^2 of different seismic phases.

Phase	Number of picks	RMS (ms)	Normalized χ^2	Picking uncertainty (ms)
Pw	1891	53	1.111	50
Ps ₂ P	495	63	1.612	50
Ps ₃ P	997	75	2.281	50
Ps ₄ P	619	50	0.995	50
Ps ₃	885	92	3.377	50
Ps ₄	233	59	1.421	50
Pg	11915	95	1.126	90
Pn	1486	90	0.996	90
PmP	3379	90	1.003	90
PhP	480	63	1.612	90
Total	22648	89	1.250	

vertical grid spacings are set at 0.5 and 0.25 km, respectively. The horizontal and vertical correlation lengths are set from 3 to 10 km and from 2 to 3 km, respectively. The correlation length of the Moho reflector is 5 km. The weighting factor of velocity and depth smoothing is 50 and 5, respectively. The RMS error is 754 ms and χ^2 is 70.244 in the initial velocity model. After three iterations, the RMS error of the final inverted model is 85 ms and χ^2 is 0.89.

The distribution of high-velocity lower crustal anomalies and the Moho geometry in the final inverted model are similar with the forward modelling results. The ray coverage is shown in Fig. 7(c).

3.3 Uncertainty analysis and resolution tests

Monte Carlo method is used to analyse the inversion uncertainty (Korenaga *et al.* 2000). We generated 100 random initial velocity

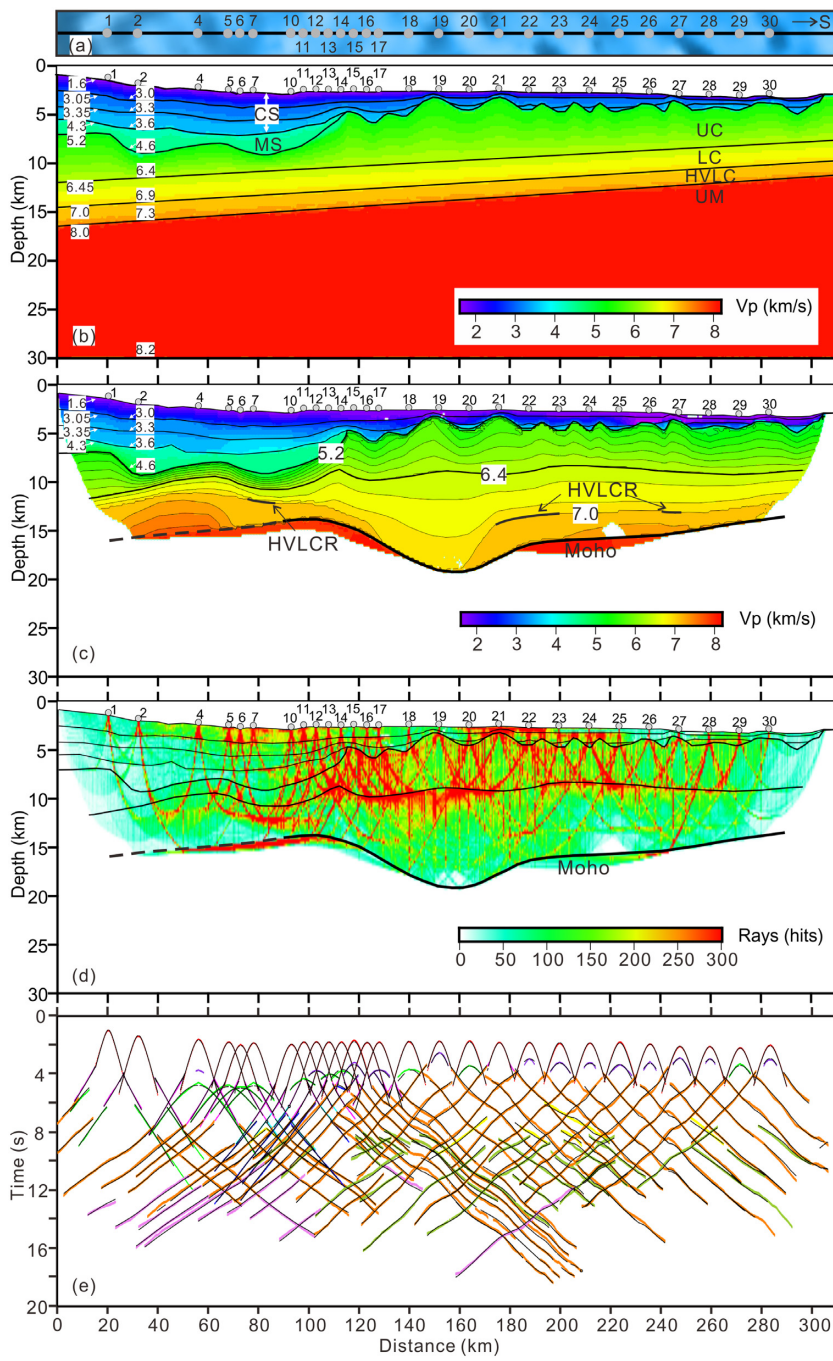


Figure 6. (a) The OBS locations in the bathymetry map. The grey dots with numbers show locations of OBSs. (b) Initial velocity model for ray tracing forward modelling. The initial velocity model includes eight velocity layers: seawater (1.5 km s^{-1}), Cenozoic sedimentary layer 1 ($1.6\text{--}3.0 \text{ km s}^{-1}$), Cenozoic sedimentary layer 2 ($3.05\text{--}3.3 \text{ km s}^{-1}$), Cenozoic sedimentary layer 3 ($3.35\text{--}3.6 \text{ km s}^{-1}$), Mesozoic sedimentary layer ($4.3\text{--}4.6 \text{ km s}^{-1}$), upper crust ($5.2\text{--}6.4 \text{ km s}^{-1}$), lower crust ($6.45\text{--}6.9 \text{ km s}^{-1}$), high-velocity lower crust ($7.0\text{--}7.3 \text{ km s}^{-1}$) and upper mantle ($8.0\text{--}8.2 \text{ km s}^{-1}$). CS, Cenozoic sediment; MS, Mesozoic sediment; UC, upper crust; LC, lower crust; HVLC, high-velocity lower crust; UM, upper mantle. The contour interval is 0.2 km s^{-1} . The thick black curve represents the Moho interface, where dashed part (model distance $< 90 \text{ km}$) indicate a lack of PmP reflections. HVLCR: top of high-velocity lower crustal layer constrained by PhP phases. (c) The final forward P -wave velocity model. The grey dots refer to the locations of OBS. The colour labels of the seismic phases are same as Fig. 3(d). (d) Ray coverage density. The dashed part of the Moho lacks PmP reflections. (e) The fitting of different seismic phases for all OBSs. The colour labels of the seismic phases are same as Fig. 3(d).

models that change only beneath the basement of Mesozoic sedimentary layer. The velocity of the top upper crust is randomly between 4.8 and 5.6 km s^{-1} , and the velocity at the model bottom is randomly between 6.8 and 8.2 km s^{-1} . The velocities in between are from linear interpolation. The initial Moho depth is randomly set between 14 and 19 km . The velocity uncertainties are mostly less than 0.06 km s^{-1} , but increase to about 0.12 km s^{-1} in the lower

part of sedimentary layer and upper crust of the Tainan Basin. The velocity uncertainties of the upper crust near the TCU increase to 0.18 km s^{-1} due to low ray coverage (Fig. 7d). The Moho depth uncertainties are mostly less than 0.2 km . Monte Carlo uncertainty analysis shows that the final inversion results are only weakly dependent on the selected initial model.

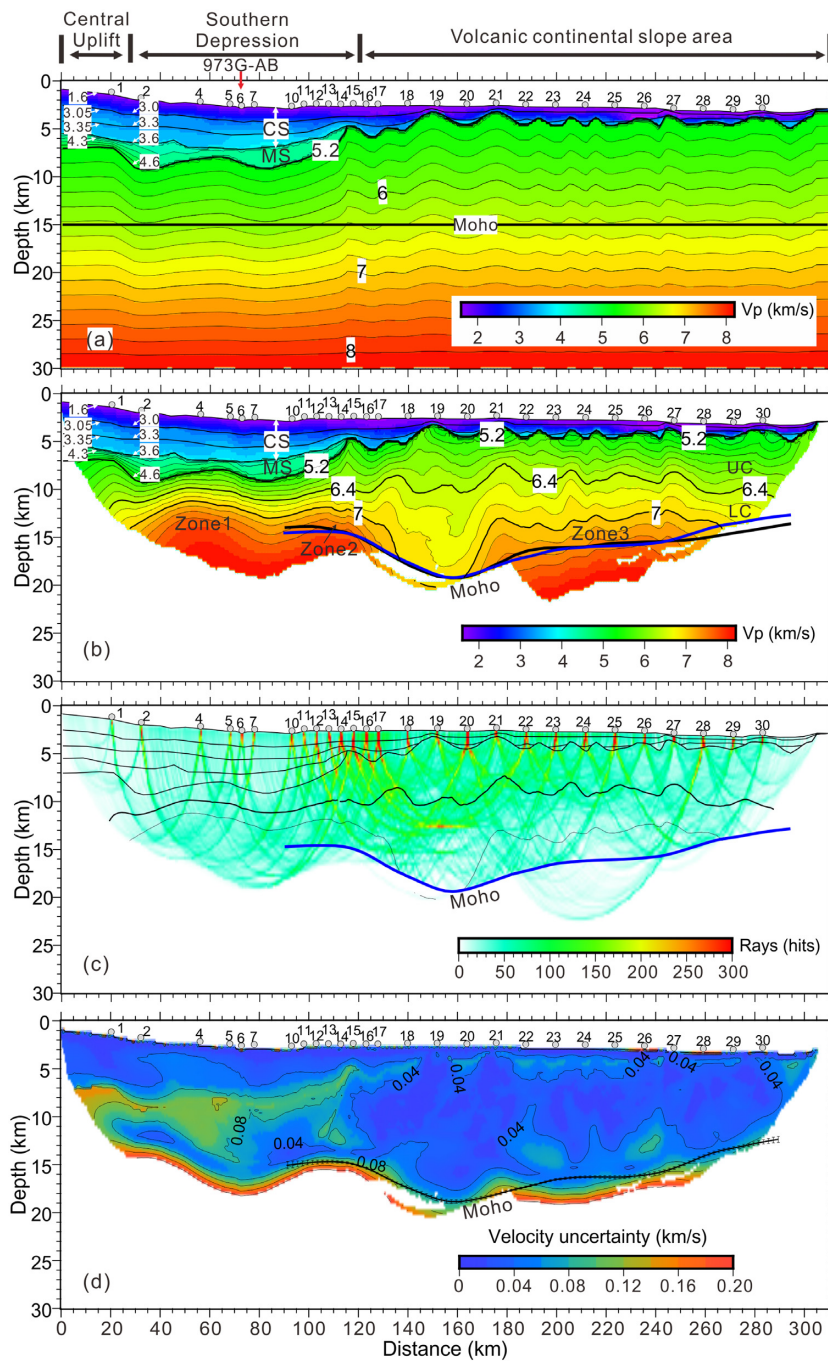


Figure 7. (a) Initial velocity model for tomographic inversion. The thick black line marks initial Moho interface. (b) Final inverted P -wave velocity model. The transect is divided into three zones, Central Uplift, Southern Depression and volcanic continental slope area. The black thick line shows the Moho from the forward model and the blue thick line shows the Moho from the inversion. CS, Cenozoic sediment; MS, Mesozoic sediment; UC, upper crust; LC, lower crust. (c) Derivative weight sum of the tomographic model. (d) Standard deviation of P -wave velocity model and Moho geometry with error bars from the Monte Carlo uncertainty analysis.

In order to evaluate the adequacy of the ray coverage and the resolution of inverted results, checkerboard resolution tests are performed with synthetic data. The checkerboard sizes are $15 \text{ km} \times 6 \text{ km}$, $10 \text{ km} \times 4 \text{ km}$ and $7.5 \text{ km} \times 3 \text{ km}$, respectively. First, we added a velocity perturbation of ± 5 per cent to the final velocity model of tomographic inversion (Fig. 7b) and took it as the forward model. Then synthetic arrival time are calculated with the same actual source-receiver survey geometry. Finally, with the initial velocity model of tomographic inversion, the synthetic arrival

time are inverted. The recoveries of velocity perturbation are shown in Fig. 8.

4 VELOCITY STRUCTURE IN THE NORTHEASTERN SCS

The Cenozoic strata in the Tainan Basin is about $3\text{--}4.5$ km thick with a velocity range from 1.6 to $3.6\text{--}3.9 \text{ km s}^{-1}$ (Fig. 7b), consistent with MCS records from Tang & Zheng (2010). The interface between the

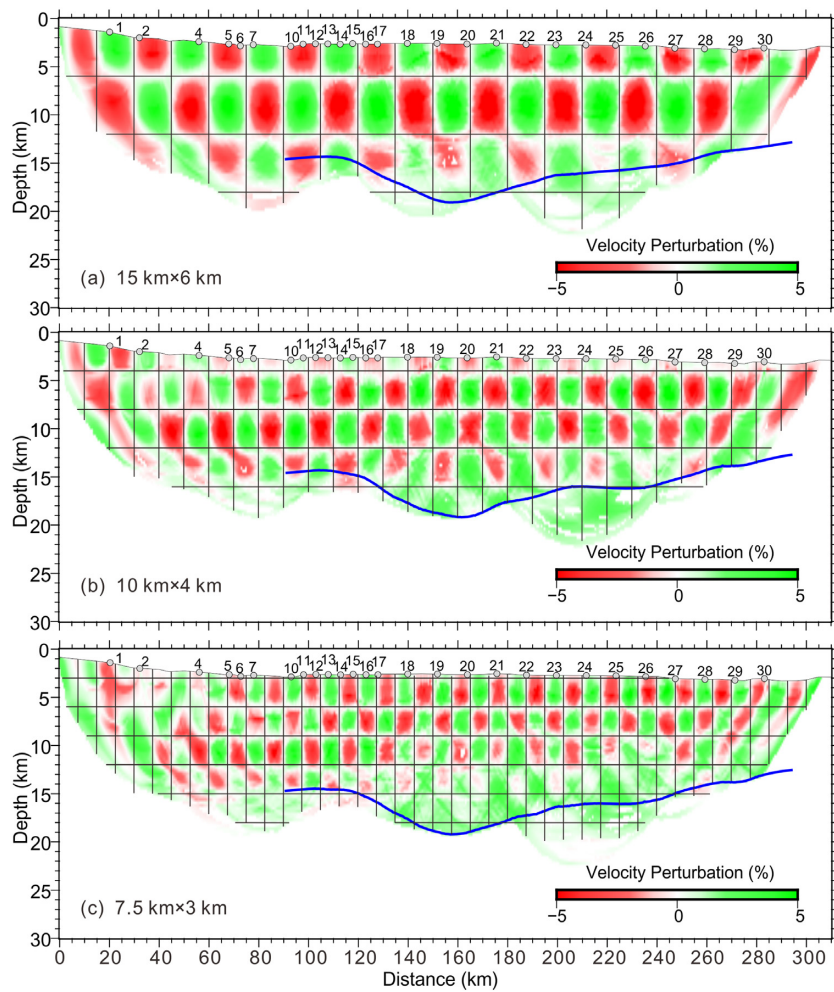


Figure 8. Recovered velocity perturbation models from checkerboard tests with grid size (a) $15 \text{ km} \times 6 \text{ km}$, (b) $10 \text{ km} \times 4 \text{ km}$, and (c) $7.5 \text{ km} \times 3 \text{ km}$. The velocity perturbation is ± 5 per cent. Blue curve shows the Moho from the tomographic inversion.

Cenozoic and Mesozoic strata has a sharp velocity change from $3.6\text{--}3.9$ to 4.3 km s^{-1} , as already found in boreholes in the Tainan Basin (Chen 2006). Mesozoic strata are mostly limited to the Tainan Basin, varying from 1 to 2.5 km in thickness, and from 4.3 to 5.2 km s^{-1} in velocity (Fig. 7b). This velocity range is identical to those revealed from boreholes (Chen & Jaw 1996; Chen 2006; Li *et al.* 2007) and from reflection seismic depth migration (Tang & Zheng 2010). The MCS line 973G-AB intersects the line OBS2019-1 and reveals the Mesozoic basement (Fig. 9).

The upper crust velocity ranges from ~ 5.0 to 6.4 km s^{-1} in the inversion model (Fig. 7b). Three high-velocity lower crustal anomalies in the P -wave velocity model are identified (Fig. 7b). High-velocity lower crustal Zone 1 is located in the centre of the TSD (model distance $25\text{--}85 \text{ km}$), with velocities of $7.0\text{--}8.0 \text{ km s}^{-1}$ and a maximum thickness of $\sim 4 \text{ km}$. High-velocity lower crustal Zone 2 is to the south of the TSD (model distance $85\text{--}135 \text{ km}$), with velocities of $7.0\text{--}7.6 \text{ km s}^{-1}$ and a thickness of $\sim 2.5 \text{ km}$. Zone 3 is located in the volcanic continental slope area further seawards (model distance $165\text{--}265 \text{ km}$), with velocities of $7.0\text{--}7.4 \text{ km s}^{-1}$ and a thickness of $\sim 2.5 \text{ km}$. In the TSD of Tainan Basin, the crust thins significantly to $\sim 6\text{--}7 \text{ km}$ (Fig. 7b). No high-velocity lower crustal anomaly is observed beneath a zone of thick crust to the south of the TSD, consistent with isostasy.

5 DISCUSSION

5.1 HVLC below the volcanic continental slope area

Previously, high-velocity lower crustal anomalies were mostly imaged as single continuous layers in different profiles in the study area (Wang *et al.* 2006; Eakin *et al.* 2014; Lester *et al.* 2014; Wan *et al.* 2017; Liu *et al.* 2018). However, Wan *et al.* (2019) recognized several isolated high-velocity lower crustal anomalies (Fig. 10a). Our profile OBS2019-1 also shows that the high-velocity lower crustal anomalies are not continuous, but are separated by a relatively thick extended continental crust (Fig. 10g). This reveals that magmatic underplating/intrusions is either locally isolated or high-velocity lower crustal anomalies are of different origins.

In order to study the property of HVLC, we extract 1-D crustal velocity-depth profiles from tomographic inversion results at 10 OBS locations, and compare them with velocity profiles from the thinned northern SCS continental crust, the Atlantic oceanic crust ($0\text{--}127 \text{ Ma}$, White *et al.* 1992, Fig. 11a), the West Iberian and Newfoundland margins (Minshull 2009, Fig. 11b) and the Central Tyrrhenian basin (Prada *et al.* 2014, Fig. 11c). The final velocity-depth profiles (Fig. 11) are derived from tomographic results, because tomographic inversion provides objective estimations of

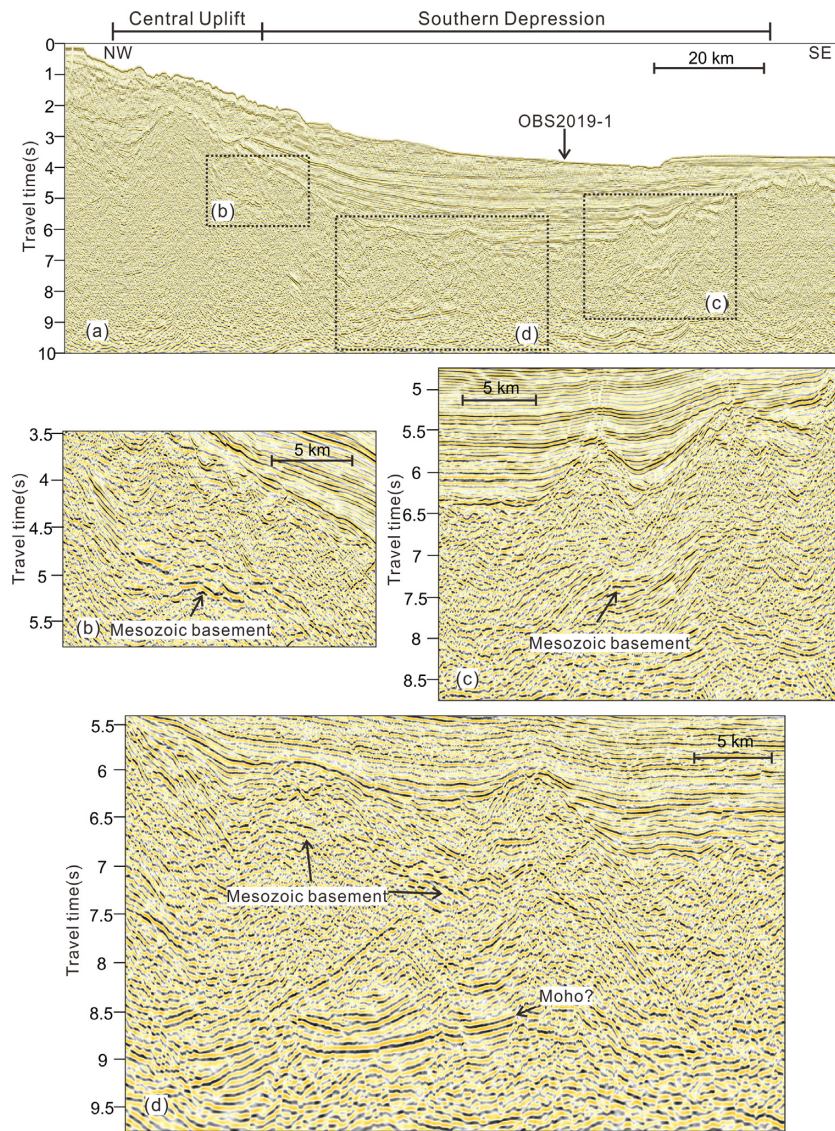


Figure 9. (a) The seismic section along line 973G-AB. (b), (c) and (d) are zoomed views of the Mesozoic basement reflections.

resolution, uncertainty and non-uniqueness compared with the trial-and-error forward modelling (Zelt & Smith 1992). The final forward models are smooth but the resolution of fine-scale features and model uncertainty are limited by the model parametrization, whereas inversion with a grid-based parametrization has proved more effective than forward modelling in constraining the P -wave velocity models (e.g. White & Smith 2009).

HVLC caused by magmatic underplating/intrusions (Nissen *et al.* 1995; Yan *et al.* 2001; Wang *et al.* 2006; Zhao *et al.* 2010; Wei *et al.* 2011; Lester *et al.* 2014; Wan *et al.* 2017) are characterized by lower velocity range ($7.0\text{--}7.4\text{ km s}^{-1}$) and lower velocity gradient than serpentinized mantle (Hou *et al.* 2019; Wan *et al.* 2019). The velocity range of high-velocity lower crustal Zone 3 is $7.0\text{--}7.4\text{ km s}^{-1}$ and its 1-D velocity-depth profiles at OBS22, OBS25 and OBS27 match well with previous results from northern SCS continental slope (Nissen *et al.* 1995; Qiu *et al.* 2001; Yan *et al.* 2001; Wang *et al.* 2006, Fig. 11a), showing evidences of magmatic underplating/intrusions. The crustal velocity gradients at OBS22, OBS25 and OBS27 of volcanic continental slope area are close to those of thinned continental crust in the northern SCS margin, but

are obviously distinguishable from those of normal oceanic crust (White *et al.* 1992, Fig. 11a).

The melt thickness depends on the preliminary thickness of lithosphere, the degree of lithosphere thinning, the potential mantle temperature and the rift duration (Bown & White 1995). Although many factors may impact the melt thickness, we assume that these factors are the same in a limited continental margin area except for the degree of lithosphere thinning. At the continental slope, the degree of lithosphere thinning, the degree of decompressive melting, and melt thickness are expected to increase seawards. However, the thicknesses of our imaged HVLC decrease seawards (Figs 10a, d), not in accordance with the characteristics of syn-rifting magmatism. No HVLC is found beneath the crust in southern China (Yin *et al.* 1999; Li *et al.* 2006), indicating that HVLC were not formed before rifting.

We apply the decompression melting model of Bown & White (1995) to test the expected melt volumes from the rifting process and study the timing and genesis of high-velocity lower crustal zones. We assume pure shear rifting and a single rifting episode lasted for $\sim 21\text{--}32$ Ma from $\sim 66\text{--}55$ Ma (Taylor & Hayes 1983; Ru

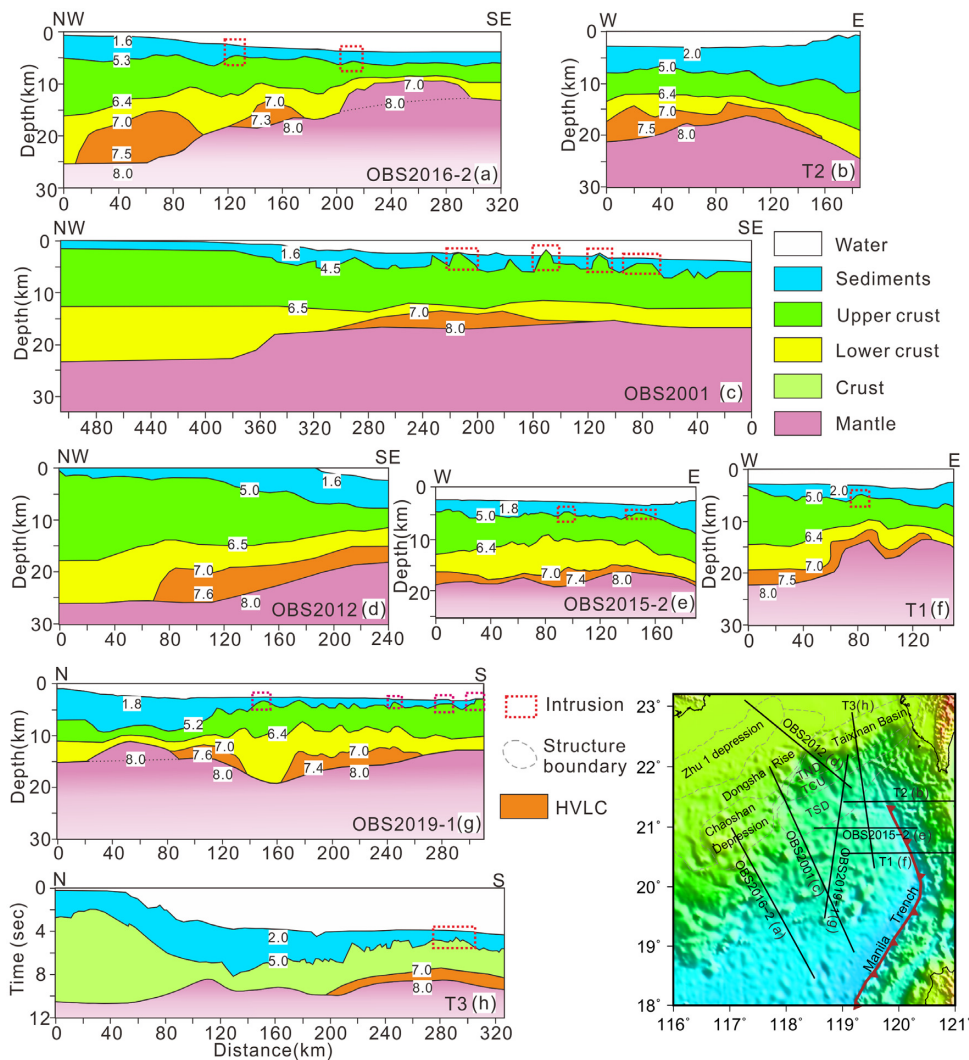


Figure 10. Crustal structure along profiles (a) OBS2016–2 (Wan *et al.* 2019), (b) T2 (Eakin *et al.* 2014), (c) OBS2001 (Wang *et al.* 2006), (d) OBS2012 (Wan *et al.* 2017), (e) OBS2015–2 (Liu *et al.* 2018), (f) T1 (Eakin *et al.* 2014), (g) OBS2019–1 and (h) T3 (Lester *et al.* 2014). The red rectangle represents the location of volcanic body or intrusion. The white labels with numbers indicate the velocity (km s^{-1}) for the main boundaries. The variation of velocity at the top upper crust is $4.5\text{--}5.3 \text{ km s}^{-1}$. The velocity at the top uppermost mantle is 8.0 km s^{-1} . The dashed lines in (a) and (g) represent the serpentization front. HVLC, high-velocity lower crust.

& Pigott 1986) to ~ 34 Ma (Li *et al.* 2014). The crustal thickness of the unstretched continental margin of the SCS is $\sim 30\text{--}35$ km (Li *et al.* 2006). We estimate that the stretching factor β is ~ 8 in the TSD and is ~ 3 in the volcanic continental slope area. Only with an anomalously high mantle temperature of up to 1480°C (White & McKenzie 1989) can high-velocity lower crustal anomalies be generated below the volcanic continental slope area (Fig. 12). However, recent geochemical and geophysical analyses showed that the continental rifting of SCS was not affected by a mantle plume (Yu & Liu 2020). Syn-rifting magmatism for a normal mantle lithosphere should be weak in the area (Fig. 12).

Timing of widespread magmatic activities in the northern margin of the SCS is controversial. Studies in the Pearl River Mouth Basin (Xie *et al.* 2017) and southwest Taiwan (Wang *et al.* 2012) showed that the magmatism are mainly after the cessation of rifting (Yeh *et al.* 2012; Franke 2013; Lester *et al.* 2014; Fan *et al.* 2017). Song *et al.* (2017) confirmed that the syn-rift and syn-spreading magmatic activities are sparse on the northern margin of the SCS, and most

magmatic features are post-spreading, as also suggested by Yan *et al.* (2006).

Volcanic body in the single-channel seismic profile coincident with OBS line is capped with sediments but it is not related to sedimentary deformation around them (Fig. 2b). Tilting and folding of strata on the flanks of the volcanic body is more likely caused by differential compression and subsidence, rather than by late magmatism (Fig. 2b). However, volcanic bodies in Figs 2(c) and (d) caused offset and deformation of sedimentary strata and seafloor, or were even exposed to the seafloor, showing evidences of post-spreading magmatism. Moreover, uplifted fault blocks caused offset and deformation of sediments and seafloor (Figs 2b and c). Adding magmatic materials to the bottom of lower crust will also cause uplift of sedimentary strata if the material is less dense than the mantle (Macلنан & Lovell 2002). We estimate that uplift are associated with post-spreading magmatic underplating/intrusions because the post-spreading sedimentary deformation caused by uplifted fault blocks spatially coincide with magmatic underplating/intrusions (Figs 2

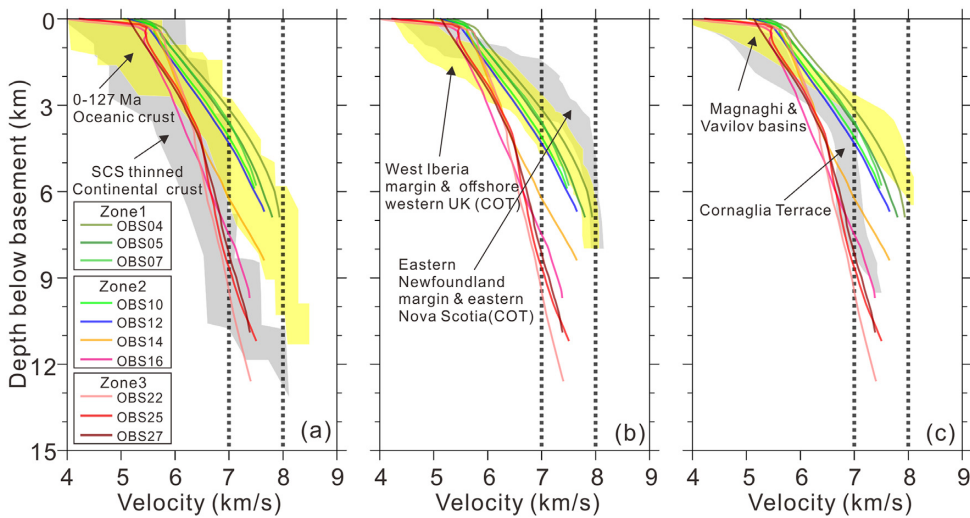


Figure 11. 1-D P -wave velocity–depth profiles at three high-velocity lower crustal zones along profile OBS2019–1. (a) Comparison with the thinned continental crust in the northern SCS margin (Nissen *et al.* 1995; Qiu *et al.* 2001; Yan *et al.* 2001; Wang *et al.* 2006) and the Atlantic oceanic crust (0–127 Ma, White *et al.* 1992). (b) Comparison with the West Iberia and Newfoundland margins (Minshull 2009). (c) Comparison with the Central Tyrrhenian basin including Magnaghi & Vavilov basins and Corniglia Terrace (Prada *et al.* 2014).

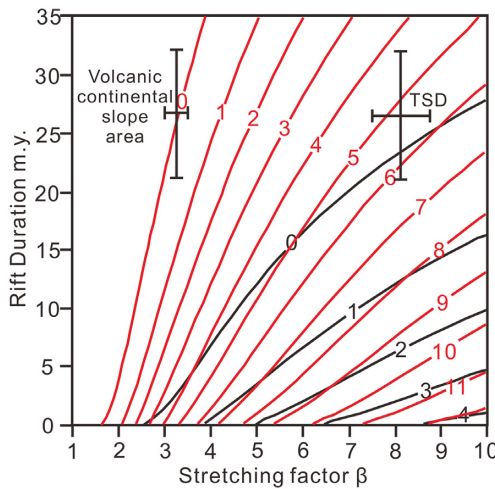


Figure 12. Variation of final syn-rift melt thickness for a continental lithosphere of initially 125 km in thickness, with different stretching factors, rift durations and potential mantle temperatures (Bown & White 1995). The numbers show the thickness of the magma produced by decompressive melting during rifting. The red and black isolines represent the melting thickness produced by a lithospheric potential mantle temperature of 1400 °C (red) and 1300 °C (black), respectively. TSD: Tainan Southern Depression.

and 7b). Therefore, syn-rifting and syn-spreading magmatic activities are not dominant in our research area, and most magmatism occurred during post-spreading.

The distribution of the HVLC in the northeastern SCS indicates a more local origin. HVLC exist primarily in the east part of northern continental margin of the SCS but not in the west. Neither a regional mantle plume nor convective removal of continental lithosphere (Chung *et al.* 1994; Lester *et al.* 2014) can be supported. Therefore, we support that the post-spreading magmatism is most likely triggered by extension related to cooling of the oceanic and attenuated continental lithosphere (Song *et al.* 2017). This mechanism can explain the different magmatic activities between the east and west segments of northern SCS margin, and the isolated high-velocity lower crustal anomalies.

5.2 HVLC below the TSD

The velocity gradient of the high-velocity lower crustal Zone 1 from OBS04, OBS05 and OBS07 is significantly higher than that of high-velocity lower crustal Zone 3 and of the thinned continental crust in the northern SCS margin (Nissen *et al.* 1995; Qiu *et al.* 2001; Yan *et al.* 2001; Wang *et al.* 2006, Fig. 11a). The velocity and velocity gradient of the high-velocity lower crustal Zone 1 are similar with that of the West Iberian and Newfoundland margins, where mantle exhumation and serpentinization have been confirmed (Fig. 11b, Boillot *et al.* 1989; Dean *et al.* 2000; Whitmarsh *et al.* 2001; Funck *et al.* 2003; Van Avendonk *et al.* 2006; Minshull 2009). Moreover, the velocity of the high-velocity lower crustal Zone 1 increases from $V_p < 8 \text{ km s}^{-1}$ to $V_p > 8 \text{ km s}^{-1}$ in gradual transition (Fig. 7b). Thus, we suggest that the high-velocity lower crustal Zone 1 originates from peridotite serpentinization in the uppermost mantle. Magmatic underplating/intrusions can hardly dim the Moho reflection, but mantle serpentinization does (Minshull 2009; Prada *et al.* 2015). The lack of Moho reflection phases at model distance 20–90 km also indicates that the high-velocity lower crustal Zone 1 may be due to mantle serpentinization. There are many large crust-penetrating detachments or normal faults around the failed rift (Yeh *et al.* 2012; Lester *et al.* 2014; McIntosh *et al.* 2014), through which seawater could have entered into the uppermost mantle, resulting in serpentinization. From the nearby MCS profiles MGL0908–3 and MGL0905–22, we infer that the top of serpentinized mantle is probably near the 6.9 km s^{-1} velocity contour below the failed rift axis (Fig. 13b). The velocity of serpentinized mantle is estimated to increase from 6.9 to 8 km s^{-1} between 3.5 and 6 km in depth below the Mesozoic basement.

Although the velocity–depth profiles of the TSD fall into the bounds of normal oceanic crust (White *et al.* 1992, OBS04, OBS05 and OBS07 in Fig. 11a), the crust here is considered continental. The reasons include the following: This region does not show magnetic anomalies related to seafloor spreading; The velocity gradients ($ca. 0.5 \text{ s}^{-1}$) of the upper crust ($< 6.5 \text{ km s}^{-1}$) are much smaller than that of the normal oceanic crust ($ca. 1\text{--}2 \text{ s}^{-1}$); MCS profiles across the thinned crust reveal many faults and fault blocks formed by extension (Li *et al.* 2007; Yeh *et al.* 2012; Lester *et al.* 2014; McIntosh *et al.* 2014).

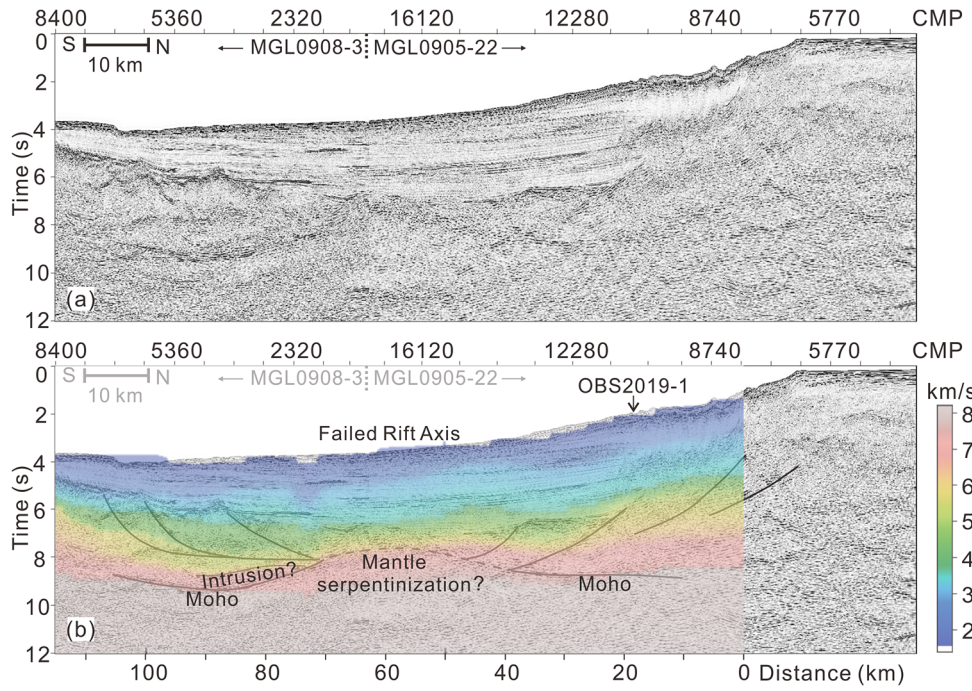


Figure 13. Spliced seismic image of MGL0908–3 and MGL0905–22 (from McIntosh *et al.* 2014, and with the permission of Elsevier). The locations of these lines are showed in Fig. 1. (a) Time-migrated seismic reflection image. (b) Interpretation with overlapped velocity profile OBS2019–1. The arrow indicates the intersecting location between profile OBS2019–1 and the MCS profiles. The dashed line indicates the lack of Moho reflection, likely caused by mantle serpentinization.

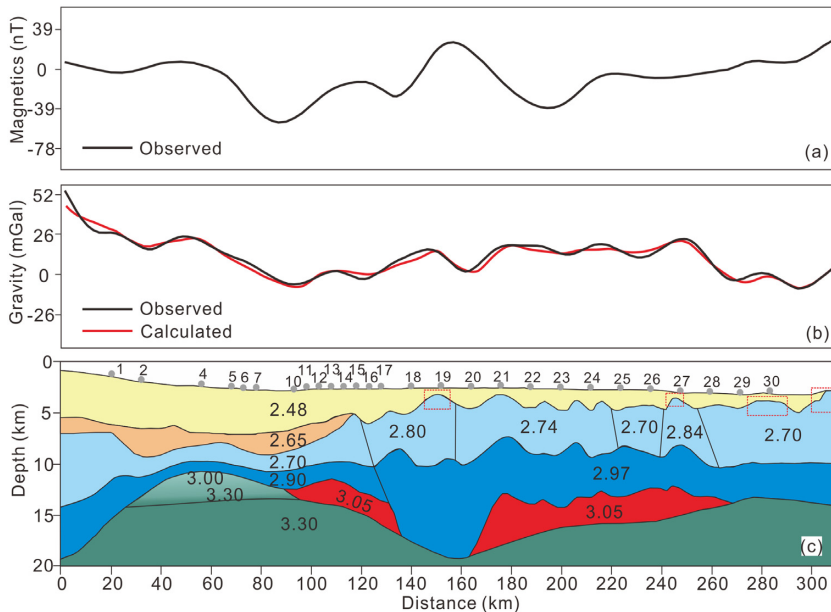


Figure 14. (a) Observed magnetic anomalies. (b) The fitting between the observed and calculated free-air gravity anomalies. (c) Density model (the unit in g cm^{-3}). The red rectangles mark the locations of volcanic bodies.

Free-air gravity anomaly (Bonvalot *et al.* 2012) and magnetic anomaly (Maus *et al.* 2009) are also analysed along the survey line to further validate serpentinization below the failed rift. The interfaces of the density model are referred to the tomographic inversion results (Fig. 7b). Based on the relationship between P -wave velocity and density for terrestrial sediments ($\rho = 0.917 + 0.747V_p - 0.08V_p^2$; Hamilton 1978), the average densities of Cenozoic and Mesozoic sediments are 2.48 and 2.65 g cm^{-3} , respectively. From

the P -wave velocity and density relationship of continental crust (Christensen & Mooney 1995), the mean density is 2.74 g cm^{-3} in the upper crust and 2.94 g cm^{-3} in the lower crust. According to the relationship between density and velocity for serpentinized peridotite ($\rho = 0.2703V_p + 1.140$; Miller & Christensen 1997), the density from the top to bottom of serpentinized upper mantle is estimated to increase from 3.00 to 3.30 g cm^{-3} .

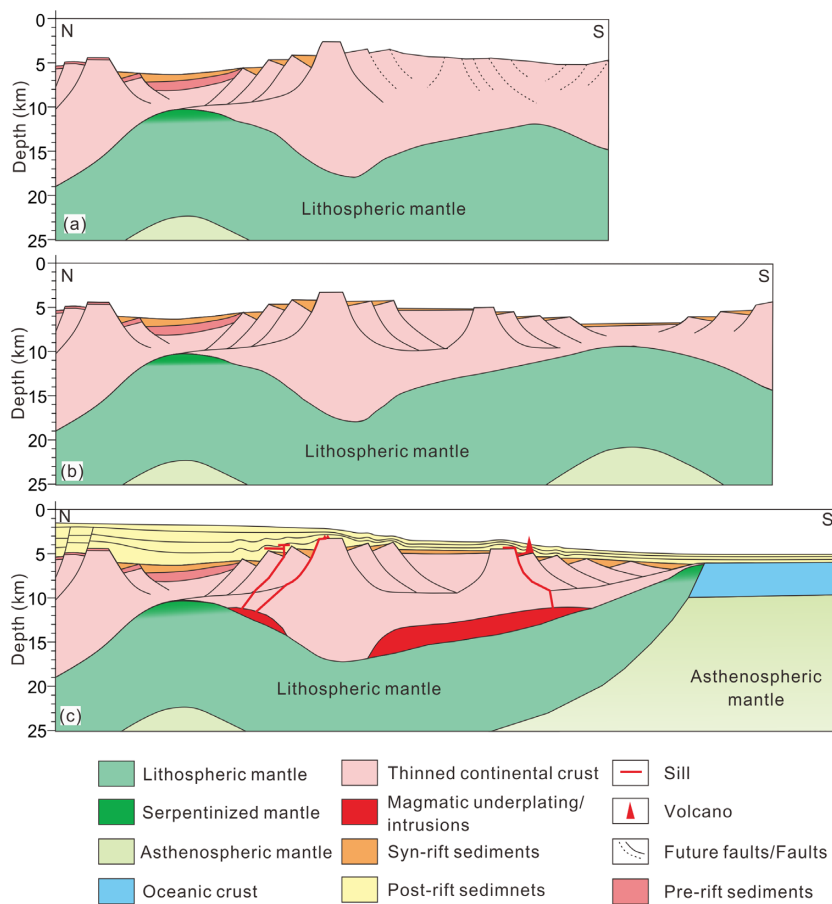


Figure 15. Conceptual reconstructions of the evolution of northeastern SCS margin. (a) Rift failed to further develop. (b) A new rift developed to the south of the initial rifting site. (c) Lithosphere breakups along the new rift to form oceanic crust, and post-spreading magmatic underplating/intrusions started to occur.

The final density model has a RMS residual of 2.75 mGal (Fig. 14c). Modelled upper crustal densities are very high at model distances 130–150 and 240–260 km, reaching above 2.80 g cm^{-3} , which may be caused by extensive magma intrusions. The upper mantle density ($3.00\text{--}3.30 \text{ g cm}^{-3}$) at model distance 20–90 km is lower than that of the normal mantle (3.30 g cm^{-3}), due to serpentinization. The corresponding magnetic anomaly also shows a local high above this interpreted high-velocity lower crustal anomaly that may have elevated magnetic susceptibilities from mantle serpentinization. According to the relationship between density and percentage of serpentinization (Miller & Christensen 1997), the degree of serpentinization here is estimated to decrease from ~ 38 per cent to 0 from the top to bottom of serpentinized upper mantle. At model distance 100–140 and 160–270 km, the densities of HVLC are 3.05 g cm^{-3} , likely from magmatic underplating/intrusions. Volcanic bodies correspond well to magnetic anomalies except for at model distance 250 km (Fig. 14), where different magnetizations of multistage magmatic intrusions can weaken the superimposed magnetic signals.

To understand the lateral transition from mantle serpentinization to magmatic underplating or intrusions, we compared velocity-depth profiles of high-velocity lower crustal Zone 1 and Zone 2 with those of Cornaglia Terrace and adjacent Magnaghi & Vavilov basins, where lateral transition also occurred (Fig. 11c). The high-velocity lower crustal anomalies ($> 7 \text{ km s}^{-1}$) under the Cornaglia Terrace originate from magmatic underplating or intrusions, whereas under the adjacent Magnaghi & Vavilov basins they

originate from serpentinized mantle (Prada *et al.* 2014, 2015). The crustal velocity gradient of high-velocity lower crustal Zone 2 is similar to that of Cornaglia Terrace (Fig. 11c). The bottom interface of high-velocity lower crustal Zone 2 is constrained by PmP reflections (Fig. 7b), and the high-velocity lower crustal Zone 2 may be caused by magmatic underplating/intrusions. The velocity gradient of high-velocity lower crustal Zone 1 is close to that of serpentinized mantle in both the western Iberian margin (Fig. 11b) and the Magnaghi & Vavilov basins (Fig. 11c). Therefore, the transition from high-velocity lower crustal Zone 2 to Zone 1 is similar to that from the Cornaglia Terrace to Magnaghi and Vavilov basins. We also infer that magmatic underplating/intrusions probably transform into serpentinized mantle at model distance ~ 90 km, where PmP phases disappear landward. The density increases from the high-velocity lower crustal Zone 2 towards Zone 1 (Fig. 14c), also indicating the lateral transition from magmatic underplating/intrusions to mantle serpentinization.

5.3 Implications for magma-poor margin formation

The northeastern SCS continental margin has experienced a complex multistage rifting history. In the TSD, the crust was severely stretched and thinned. Low-angle detachment faults or normal faults probably penetrated to the top of upwelled upper mantle, providing pathways for seawater to reach the upper mantle (Fig. 15a). Numerical simulations illustrate that crustal-scale faulting and mantle

serpentization can occur during rifting when the entire crust becomes brittle at stretching factors of 3–5 and the uppermost mantle cools below 600 °C (Pérez-Gussinyé & Reston 2001). Mantle serpentization could have occurred below the failed rift of the TSD due to high crustal stretching (stretching factors >7.5), and low mantle temperature implied by weak magmatic activities. Mantle serpentization beneath a failed rift is not unusual, as already documented in the Porcupine Basin, offshore Ireland (Reston *et al.* 2004; Prada *et al.* 2017).

The polyphase rifting in the northern margin of the SCS migrated from north to south (Ru & Pigott 1986, Sun *et al.* 2009), similar to rift migration in the Northeastern Atlantic margins (Reemst & Cloetingh 2000; Naliboff & Buiter 2015). The failed rift formed in the TSD first, and then rifting migrated to the location of final lithospheric breakup (Fig. 15b). After the first phase of extension (Fig. 15a), conductive cooling may increase the integrated strength of the initial rift. At this stage, the initial rift can be abandoned and extension shifts to weaker and warmer areas outside the rift flanks (van Wijk & Cloetingh 2002; Naliboff & Buiter 2015).

A new rift formed ~200 km away from the failed rift (Fig. 15b), and at this position the lithosphere broke up and a seafloor spreading system evolved (Fig. 15c). After the cessation of seafloor spreading, due to extension related to cooling and thermal contraction of oceanic and attenuated continental lithosphere, decompressive melting occurred under the continental slope, forming isolated high-velocity lower crustal anomalies. Magma can also reach the upper part of crust along faults, forming sills, dikes and volcanoes (Fig. 15c).

6 CONCLUSIONS

This paper provides new insights into the crustal structure and magmatic activities at the northeastern continental margin of the SCS, based on seismic, gravity and magnetic data.

A high-resolution velocity model of line OBS2019–1 is obtained by forward modelling and tomographic inversion. The velocity model reveals Mesozoic strata in the Tainan Basin that gradually pinched out towards the volcanic continental slope, with a velocity range of about 4.3–5.2 km s⁻¹. In the TSD, the crustal thickness is severely thinned to ~4 km. In the volcanic continental slope area, the crustal thickness decreases from 15 to 10 km seawards.

The high-velocity lower crustal anomalies in the northeastern SCS are isolated, and are largely absent beneath thick extended continental crust in the continental slope. We divide high-velocity lower crustal anomalies into three zones according to its characteristics. The high-velocity and velocity gradient, as well as lack of PmP reflections, indicate that the high-velocity lower crustal Zone 1 may be caused by mantle serpentization below the failed rift. The velocity range and the presence of PmP reflections support that the high-velocity lower crustal Zones 2 and 3 beneath the continental slope may be caused by post-spreading magmatic underplating or intrusions. At model distance ~90 km, lateral transition from magmatic underplating or intrusions to mantle serpentization occurred abruptly.

The magmatic underplating or intrusions spatially coincide with the post-spreading sedimentary deformation and magmatism. Syn-rifting and syn-spreading magmatic activities are not dominant in the northeastern SCS margin, and most of the magmatic activities are post-spreading.

We have found that in the magma-poor margin, serpentized mantle can occur not only in the COT region, but also below the rift

during early-stage rifting. The limited magmatic activities during rifting and the serpentized mantle found below the failed rift basin argue for a magma-poor continental margin in northeastern SCS.

ACKNOWLEDGEMENTS

We are grateful to Dieter Franke and Zhen Sun for their fruitful comments and constructive suggestions. Seismic data acquisition was supported by Chinese Natural Science Foundation Open Research Cruise (Cruise No. NORC2019–08). We thank the officers and crew of R/V ‘Shiyan-2’ of South China Sea Institute of Oceanology, Chinese Academy of Sciences for their contributions. This study was supported by National Natural Science Foundation of China (Grant Nos. 41776057, 41761134051, 91858213, 41730532 and 91428039). Data processing and mapping are supported by software GMT (Wessel & Smith 1998), Rayinvr (Zelt & Smith 1992) and Tomo2D (Korenaga *et al.* 2000). Data presented in this study can be obtained from Chun-Feng Li (cfli@zju.edu.cn) and Yutao Liu (e-mail: 11834032@zju.edu.cn).

REFERENCES

- Boillot, G., Féraud, G., Recq, M. & Girardeau, J., 1989. Undercrusting by serpentinite beneath rifted margins, *Nature*, **341**, 523–525.
- Bonvalot, S. *et al.*, 2012. *World Gravity Map*, Commission for the Geological Map of the World, BGI-CGMW-CNRS-IRD, Paris.
- Bown, J.W. & White, R.S., 1995. Effect of finite extension rate on melt generation at rifted continental margins, *J. geophys. Res.*, **100**(B9), 18 011–18 029.
- Briais, A., Patriat, P. & Tapponnier, P., 1993. Updated interpretation of magnetic anomalies and seafloor spreading stages in the south china sea: implications for the tertiary tectonics of Southeast Asia, *J. geophys. Res.*, **98**(B4), 6299–6328.
- Chen, M.L., 2006. Sediment velocity structures in the Taiwan Strait and the coastal plain of west Taiwan. *Master thesis*, Institute of Geophysics, National Central University, Taiwan.
- Chen, A.T. & Jaw, Y.-S., 1996. Velocity structure near the northern Manila trench: an OBS refraction survey, *TAO*, **7**, 277–297.
- Christensen, N. & Mooney, W., 1995. Seismic velocity structure and composition of the continental crust: a global view, *J. geophys. Res.*, **100**(B7), 9761–9788.
- Chung, S.L., Sun, S.S., Tu, K., Chen, C.H. & Lee, C.Y., 1994. Late Cenozoic basaltic volcanism around the Taiwan Strait, SE China: Product of lithosphere-asthenosphere interaction during continental extension, *Chem. Geol.*, **112**(1–2), 1–20.
- Dean, S.M., Minshull, T.A., Whitmarsh, R.B. & Louden, K.E., 2000. Deep structure of the ocean-continent transition in the southern Iberia Abyssal Plain from seismic refraction profiles: the IAM-9 transect at 40°20'N, *J. geophys. Res.*, **105**(B3), 5859–5885.
- Eakin, D.H., McIntosh, K.D., Van Avendonk, H.J.A., Lavier, L., Lester, R., Liu, C.-S. & Lee, C.-S., 2014. Crustal-scale seismic profiles across the Manila subduction zone: the transition from intraoceanic subduction to incipient collision, *J. Geophys. Res. Solid Earth*, **119**, 1–17.
- Funck, T., Hopper, J.R., Larsen, H.C., Louden, K.E., Tucholke, B.E. & Holbrook, W.S., 2003. Crustal structure of the ocean-continent transition at Flemish Cap: Seismic refraction results, *J. geophys. Res.*, **108**(B11), 2531.
- Fan, C., Xia, S., Zhao, F., Sun, J., Cao, J., Xu, H. & Wan, K., 2017. New insights into the magmatism in the northern margin of the South China Sea: Spatial features and volume of intraplate seamounts, *Geochim. Geophys. Geosyst.*, **18**, 2216–2239.
- Franke, D., 2013. Rifting, lithosphere breakup and volcanism: Comparison of magma-poor and volcanic rifted margins, *Mar. Pet. Geol.*, **43**, 63–87.
- Hamilton, E.L., 1978. Sound velocity-density relations in sea-floor sediments and rocks, *J. acoust. Soc. Am.*, **63**(2), 366–377.

- Hou, W.A., Li, C.-F., Wan, X.L., Zhao, M.H. & Qiu, X.L., 2019. Crustal S-wave velocity structure across the northeastern South China Sea continental margin: implications for lithology and mantle exhumation, *Earth Planet. Phys.*, **3**(4), 313–328.
- Korenaga, J., Holbrook, W.S., Kent, G.M., Kelemen, P.B., Detrick, R.S., Larsen, H.C., Hopper, J.R. & Dahl-Jensen, T., 2000. Crustal structure of the southeast Greenland margin from joint refraction and reflection seismic tomography, *J. geophys. Res.*, **105**(B9), 21 591–21 614.
- Lester, R., Van Avendonk, H.J.A., McIntosh, K., Lavier, L., Liu, C.-S., Wang, T.K. & Wu, F., 2014. Rifting and magmatism in the northeastern South China Sea from wide-angle tomography and seismic reflection imaging, *J. geophys. Res.*, **119**, 2305–2323.
- Li, S., Mooney, W.D. & Fan, J., 2006. Crustal structure of mainland China from deep seismic sounding data, *Tectonophysics*, **420**, 239–252.
- Li, C.-F., Zhou, Z., Li, J., Hao, H. & Geng, J., 2007. Structures of the northeasternmost South China Sea continental margin and ocean basin: Geophysical constraints and tectonic implications, *Mar. Geophys. Res.*, **28**, 59–79.
- Li, C.-F. et al., 2014. Ages and magnetic structures of the South China Sea constrained by deep tow magnetic surveys and IODP Expedition 349, *Geochem. Geophys. Geosyst.*, **15**, 4958–4983.
- Li, Y. et al., 2020. Numerical modeling of failed rifts in the northern South China Sea margin: implications for continental rifting and breakup, *J. Asian Earth Sci.*, **199**, doi:10.1016/j.jseas.2020.104402.
- Lin, A.T. et al., 2008. Tectonic features associated with the overriding of an accretionary wedge on top of a rifted continental margin: an example from Taiwan, *Mar. Geol.*, **255**, 186–203.
- Liu, S. et al., 2018. Geophysical constraints on the lithospheric structure in the northeastern South China Sea and its implications for the South China Sea geodynamics, *Tectonophysics*, **742–743**, 101–119.
- Lüdmann, T. & Wong, H.K., 1999. Neotectonic regime on the passive continental margin of the northern South China Sea, *Tectonophysics*, **311**(1), 113–138.
- Lüdmann, T., Wong, H.K. & Wang, P., 2001. Plio-Quaternary sedimentation processes and neotectonics of the northern continental margin of the South China Sea, *Mar. Geol.*, **172**(3–4), 331–358.
- MacLennan, J. & Lovell, B., 2002. Control of regional sea level by surface uplift and subsidence caused by magmatic underplating of earth's crust, *Geology*, **30**(8), doi:10.1130/0091-7613(2002)030<0675:CORSLB>2.0.CO;2.
- Maus, S., Barckhausen, U., Berkenbosch, H., Bournas, N. & Tontini, C., 2009. EMAG2: a 2-arc min resolution earth magnetic anomaly grid compiled from satellite, airborne, and marine magnetic measurements, *Geochem. Geophys. Geosyst.*, **10**, Q08005, doi:10.1029/2009GC002471.
- McIntosh, K., Lavier, L., van Avendonk, H., Lester, R., Eakin, D. & Liu, C., 2014. Crustal structure and inferred rifting processes in the northeast South China Sea, *Mar. Pet. Geol.*, **58**, 612–626.
- Miller, D.J. & Christensen, N.I., 1997. Seismic velocities of lower crustal and upper mantle rocks from the slow-spreading Mid-Atlantic ridge, South of the Kane transform zone (MARK), *Proc. Ocean Drill. Prog. Sci. Results*, **153**, 437–454.
- Minshull, T.A., 2009. Geophysical characterisation of the ocean-continent transition at magma-poor rifted margins, *C.R. Geosci.*, **341**(5), 382–393.
- Naliboff, J. & Buiter, S.J.H., 2015. Rift reactivation and migration during multiphase extension, *Earth planet. Sci. Lett.*, **421**, 58–67.
- Nissen, S.S., Hayes, D.E., Buhl, P., Diebold, J., Yao, B., Zeng, W. & Chen, Y., 1995. Deep penetrating seismic sounding across the northern margin of the South China Sea, *J. geophys. Res.*, **100**(B11), 22407–22433.
- Pérez-Gussinyé, M. & Reston, T.J., 2001. Rheological evolution during extension at nonvolcanic rifted margins: onset of serpentinisation and development of detachments leading to continental breakup, *J. geophys. Res.*, **106**, 3961–3975.
- Prada, M., Sallares, V., Ranero, C.R., Vendrell, M.G., Grevemeyer, I., Zitellini, N. & de Franco, R., 2014. Seismic structure of the Central Tyrrhenian basin: geophysical constraints on the nature of the main crustal domains, *J. geophys. Res.*, **119**(1), 52–70.
- Prada, M., Sallares, V., Ranero, C.R., Vendrell, M.G., Grevemeyer, I., Zitellini, N. & de Franco, R., 2015. The complex 3-D transition from continental crust to backarc magmatism and exhumed mantle in the Central Tyrrhenian basin, *Geophys. J. Int.*, **203**(1), 63–78.
- Prada, M. et al., 2017. Crustal strain-dependent serpentinisation in the Porcupine Basin, offshore Ireland, *Earth planet. Sci. Lett.*, **474**, 148–159.
- Qiu, X., Ye, S., Wu, S., Shi, X., Zhou, D., Xia, K. & Flueh, E.R., 2001. Crustal structure across the xisha trough, northwestern South China Sea, *Tectonophysics*, **341**, 179–193.
- Reemst, P. & Cloetingh, S., 2000. Polyphase rift evolution of the Voring margin (mid-Norway): constraints from forward tectonostratigraphic modeling, *Tectonics*, **19**(2), 225–240.
- Reston, T.J., Gaw, V., Pennell, J., Klaeschen, D., Stubenrauch, A. & Walker, I., 2004. Extreme crustal thinning in the south Porcupine Basin and the nature of the Porcupine Median High: implications for the formation of non-volcanic rifted margins, *J. Geol. Soc.*, **161**(5), 783–798.
- Ru, K. & Pigott, J.D., (1986). Episodic rifting and subsidence in the South China Sea, *AAPG Bull.*, **70**(9), 1136–1155.
- Shi, H.S. & Li, C.-F., 2012. Mesozoic and early Cenozoic tectonic convergence-to-rifting transition prior to opening of the South China Sea, *Int. Geol. Rev.*, **54**(15), 1801–1828.
- Song, T., Li, C., Wu, S., Yao, Y. & Gao, J., 2019. Extensional styles of the conjugate rifted margins of the South China Sea, *J. Asian Earth Sci.*, **177**, 117–128.
- Song, X.X., Li, C.-F., Yao, Y.J. & Shi, H.-S., 2017. Magmatism in the evolution of the South China sea: geophysical characterization, *Mar. Geol.*, **394**, 4–15.
- Sun, Z., Zhong, Z., Keep, M., Zhou, D., Cai, D., Li, X., Wu, S. & Jiang, J., 2009. 3D analogue modeling of the South China Sea: a discussion on breakup pattern, *J. Asian Earth Sci.*, **34**(4), 544–556.
- Sun, Z., Lin, J., Qiu, N., Jian, Z., Wang, P., Pang, X., Zheng, J. & Zhu, B., 2019. The role of magmatism in the thinning and breakup of the South China Sea continental margin, *Natl. Sci. Rev.*, **6**(5), 871–876.
- Tang, Q.S. & Zheng, C., 2010. Seismic velocity structure and improved seismic image of the southern depression of the Tainan basin from pre-stack depth migration, *Terrest. Atmos. Oceanic Sci.*, **21**(5), 807–816.
- Taylor, B. & Hayes, D.E., 1980. The tectonic evolution of the South China Basin, in *The Tectonic and Geologic Evolution of Southeast Asian Seas and Islands, Part I*, Vol. 23, Geophysical Monograph Series, ed. Hayes , D.E., pp. 89–104, American Geophysical Union.
- Taylor, B. & Hayes, D.E., 1983. Origin and history of the South China Sea basin. *The Tectonic and Geologic Evolution of Southeast Asian Seas and Islands, Part II*, Vol. 27, Geophysical Monograph Series, ed., Hayes, D.E., pp. 23–56, American Geophysical Union.
- Van Avendonk, H.J.A., Holbrook, W.S., Nunes, G.T., Shillington, D.J., Tucholke, B.E., Louden, K.E., Larsen, H.C. & Hopper, J.R., 2006. Seismic velocity structure of the rifted margin of the eastern Grand Banks of Newfoundland, Canada, *J. geophys. Res.*, **111**, B11404.
- van Wijk, J.W. & Cloetingh, S.A.P.L., 2002. Basin migration caused by slow lithospheric extension, *Earth planet. Sci. Lett.*, **198**(3), 275–288.
- Wan, K., Xia, S., Cao, J., Sun, J. & Xu, H., 2017. Deep seismic structure of the northeastern South China Sea: origin of a high-velocity layer in the lower crust, *J. geophys. Res.*, **122**, 2831–2858.
- Wan, X., Li, C.-F., Zhao, M., He, E., Liu, S., Qiu, X., Lu, Y. & Chen, N., 2019. Seismic velocity structure of the magnetic quiet zone and continent-ocean boundary in the northeastern South China Sea, *J. geophys. Res.*, **124**, 11 866–11 899.
- Wang, T.K., Chen, M.K., Lee, C.S. & Xia, K.Y., 2006. Seismic imaging of the transitional crust across the northeastern margin of the South China Sea, *Tectonophysics*, **412**, 237–254.
- Wang, K.-L., Lo, Y.-M., Chung, S.-L., Lo, C.-H., Hsu, S.-H., Yang, H.-J. & Shinjo, R., 2012. Age and geochemical features of dredged basalts from offshore SW Taiwan: the coincidence of intra-plate magmatism with the spreading South China Sea, *Terr. Atmos. Ocean. Sci.*, **23**(6), 657–669.
- Wei, X.D., Ruan, A.G., Zhao, M.H., Qiu, X.L., Li, J.B., Zhu, J.J., Wu, Z.L. & Ding, W.W., 2011. A wide-angle OBS profile across Dongsha uplift and Chaoshan depression in the mid-northern South China Sea. *Chin. J. Geophys. (in Chinese)*, **54**(12), 3325–3335.
- Wessel, P. & Smith, W.H.F., 1998. New, improved version of generic mapping tools released, *EOS, Trans. Am. Geophys. Un.*, **79**(47), 579.

- White, R. & McKenzie, D., 1989. Magmatism at rift zones: the generation of volcanic continental margins and flood basalts, *J. geophys. Res.*, **94**(B6), 7685.
- White, R.S., McKenzie, D. & O'Nions, R.K., 1992. Oceanic crustal thickness from seismic measurements and rare earth element inversions. *J. geophys. Res.*, **97**(B13), 19 683–19 715.
- White, R.S. & Smith, L.K., 2009. Crustal structure of the Hatton and the conjugate east Greenland rifted volcanic continental margins, NE Atlantic. *J. geophys. Res.*, **114**(B2), B02305, doi:10.1029/2008JB005856.
- Whitmarsh, R.B., Manatschal, G. & Minshull, T.A., 2001. Evolution of magma-poor continental margins from rifting to seafloor spreading, *Nature*, **413**(6852), 150–154.
- Xie, Z., Sun, L., Pang, X., Zheng, J. & Sun, Z., 2017. Origin of the Dongsha Event in the South China Sea, *Mar. Geophys. Res.*, **38**(4), 357–371.
- Yan, P., Zhou, D. & Liu, Z., 2001. A crustal structure profile across the northern continental margin of the South China Sea, *Tectonophysics*, **338**(1), 1–21.
- Yan, P., Deng, H., Liu, H., Zhang, Z. & Jiang, Y., 2006. The temporal and spatial distribution of volcanism in the South China Sea region, *J. Asian Earth Sci.*, **27**(5), 647–659.
- Yeh, Y., Hsu, S., Doo, W., Sibuet, J., Liu, C. & Lee, C., 2012. Crustal features of the northeastern South China Sea: insights from seismic and magnetic interpretations, *Mar. Geophys. Res.*, **33**(4), 307–326.
- Yin, Z.X., Lai, M.H., Xiong, S.B., Liu, H.B., Teng, J.W. & Kong, X.R., 1999. Crustal structure and velocity distribution from deep seismic sounding along the profile of Lianxian-Boluo-Gangkou in South China, *Chin. J. Geophys. (in Chinese)*, **42**(3), 383–392.
- Yu, X. & Liu, Z., 2020. Non-mantle-plume process caused the initial spreading of the South China Sea. *Sci. Rep.*, **10**, 8500.
- Zelt, C.A. & Smith, R.B., 1992. Seismic traveltimes inversion for 2-D crustal velocity structure, *Geophys. J. Int.*, **108**(1), 16–34.
- Zhao, M., Qiu, X., Xia, S., Xu, H., Wang, P., Wang, T.-K., Lee, C.-S. & Xia, K., 2010. Seismic structure in the northeastern South China Sea: S-wave velocity and Vp/Vs ratios derived from three-component OBS data, *Tectonophysics*, **480**(1–4), 183–197.
- Zhou, D., Sun, Z., Chen, H., Xu, H., Wang, W., Pang, X., Cai, D. & Hu, D., 2008. Mesozoic paleogeography and tectonic evolution of South China Sea and adjacent areas in the context of Tethyan and Paleo-Pacific interconnections, *Island Arc*, **17**(2), 186–207.
- Zhou, D., Wang, W., Wang, J., Pang, X., Cai, D. & Sun, Z., 2006. Mesozoic subduction-accretion zone in northeastern South China Sea inferred from geophysical interpretations, *Sci. China, D*, **49**(5), 471–482.

SUPPORTING INFORMATION

Supplementary data are available at *GJI* online.

Figure S1. (a) Seismic records and picked phases of the vertical component of OBS02 with a reduction velocity of 6.0 km s^{-1} . (b) The ray tracing paths. Ray paths in different colours correspond to different phases in (c). (c) The traveltime fitting (black) of picked phases.

Figure S2. (a) Seismic records and picked phases of the vertical component of OBS04 with a reduction velocity of 6.0 km s^{-1} . (b) The ray tracing paths. Ray paths in different colours correspond to different phases in (c). (c) The traveltime fitting (black) of picked phases.

Figure S3. (a) Seismic records and picked phases of the vertical component of OBS05 with a reduction velocity of 6.0 km s^{-1} . (b) The ray tracing paths. Ray paths in different colours correspond to different phases in (c). (c) The traveltime fitting (black) of picked phases.

Figure S4. (a) Seismic records and picked phases of the vertical component of OBS06 with a reduction velocity of 6.0 km s^{-1} . (b) The ray tracing paths. Ray paths in different colours correspond to

different phases in (c). (c) The traveltime fitting (black) of picked phases.

Figure S5. (a) Seismic records and picked phases of the vertical component of OBS07 with a reduction velocity of 6.0 km s^{-1} . (b) The ray tracing paths. Ray paths in different colours correspond to different phases in (c). (c) The traveltime fitting (black) of picked phases.

Figure S6. (a) Seismic records and picked phases of the vertical component of OBS11 with a reduction velocity of 6.0 km s^{-1} . (b) The ray tracing paths. Ray paths in different colours correspond to different phases in (c). (c) The traveltime fitting (black) of picked phases.

Figure S7. (a) Seismic records and picked phases of the vertical component of OBS12 with a reduction velocity of 6.0 km s^{-1} . (b) The ray tracing paths. Ray paths in different colours correspond to different phases in (c). (c) The traveltime fitting (black) of picked phases.

Figure S8. (a) Seismic records and picked phases of the vertical component of OBS13 with a reduction velocity of 6.0 km s^{-1} . (b) The ray tracing paths. Ray paths in different colours correspond to different phases in (c). (c) The traveltime fitting (black) of picked phases.

Figure S9. (a) Seismic records and picked phases of the vertical component of OBS14 with a reduction velocity of 6.0 km s^{-1} . (b) The ray tracing paths. Ray paths in different colours correspond to different phases in (c). (c) The traveltime fitting (black) of picked phases.

Figure S10. (a) Seismic records and picked phases of the vertical component of OBS15 with a reduction velocity of 6.0 km s^{-1} . (b) The ray tracing paths. Ray paths in different colours correspond to different phases in (c). (c) The traveltime fitting (black) of picked phases.

Figure S11. (a) Seismic records and picked phases of the vertical component of OBS16 with a reduction velocity of 6.0 km s^{-1} . (b) The ray tracing paths. Ray paths in different colours correspond to different phases in (c). (c) The traveltime fitting (black) of picked phases.

Figure S12. (a) Seismic records and picked phases of the vertical component of OBS17 with a reduction velocity of 6.0 km s^{-1} . (b) The ray tracing paths. Ray paths in different colours correspond to different phases in (c). (c) The traveltime fitting (black) of picked phases.

Figure S13. (a) Seismic records and picked phases of the vertical component of OBS18 with a reduction velocity of 6.0 km s^{-1} . (b) The ray tracing paths. Ray paths in different colours correspond to different phases in (c). (c) The traveltime fitting (black) of picked phases.

Figure S14. (a) Seismic records and picked phases of the vertical component of OBS19 with a reduction velocity of 6.0 km s^{-1} . (b) The ray tracing paths. Ray paths in different colours correspond to different phases in (c). (c) The traveltime fitting (black) of picked phases.

Figure S15. (a) Seismic records and picked phases of the vertical component of OBS21 with a reduction velocity of 6.0 km s^{-1} . (b) The ray tracing paths. Ray paths in different colours correspond to different phases in (c). (c) The traveltime fitting (black) of picked phases.

Figure S16. (a) Seismic records and picked phases of the vertical component of OBS22 with a reduction velocity of 6.0 km s^{-1} . (b) The ray tracing paths. Ray paths in different colours correspond to different phases in (c). (c) The traveltime fitting (black) of picked phases.

Figure S17. (a) Seismic records and picked phases of the vertical component of OBS23 with a reduction velocity of 6.0 km s^{-1} . (b) The ray tracing paths. Ray paths in different colours correspond to different phases in (c). (c) The traveltime fitting (black) of picked phases.

Figure S18. (a) Seismic records and picked phases of the vertical component of OBS24 with a reduction velocity of 6.0 km s^{-1} . (b) The ray tracing paths. Ray paths in different colours correspond to different phases in (c). (c) The traveltime fitting (black) of picked phases.

Figure S19. (a) Seismic records and picked phases of the vertical component of OBS25 with a reduction velocity of 6.0 km s^{-1} . (b) The ray tracing paths. Ray paths in different colours correspond to different phases in (c). (c) The traveltime fitting (black) of picked phases.

Figure S20. (a) Seismic records and picked phases of the vertical component of OBS26 with a reduction velocity of 6.0 km s^{-1} . (b) The ray tracing paths. Ray paths in different colours correspond to different phases in (c). (c) The traveltime fitting (black) of picked phases.

Figure S21. (a) Seismic records and picked phases of the vertical component of OBS27 with a reduction velocity of 6.0 km s^{-1} . (b)

The ray tracing paths. Ray paths in different colours correspond to different phases in (c). (c) The traveltime fitting (black) of picked phases.

Figure S22. (a) Seismic records and picked phases of the vertical component of OBS28 with a reduction velocity of 6.0 km s^{-1} . (b) The ray tracing paths. Ray paths in different colours correspond to different phases in (c). (c) The traveltime fitting (black) of picked phases.

Figure S23. (a) Seismic records and picked phases of the vertical component of OBS29 with a reduction velocity of 6.0 km s^{-1} . (b) The ray tracing paths. Ray paths in different colours correspond to different phases in (c). (c) The traveltime fitting (black) of picked phases.

Figure S24. (a) Seismic records and picked phases of the hydrophone component of OBS30 with a reduction velocity of 6.0 km s^{-1} . (b) The ray tracing paths. Ray paths in different colours correspond to different phases in (c). (c) The traveltime fitting (black) of picked phases.

Please note: Oxford University Press is not responsible for the content or functionality of any supporting materials supplied by the authors. Any queries (other than missing material) should be directed to the corresponding author for the paper.